Behavior of GFRP Reinforced Concrete Members under Combined Bending Moment and Low Axial Load

Alireza Sadat Hosseini[1]; Senthil Kumar Velkumar[2]; and Pedram Sadeghian[3]

[1] Research Assistant, Department of Civil and Resource Engineering, Dalhousie University, Halifax, NS, Canada.

(Corresponding Author, email: asadat@dal.ca)

[2] Former MASc Student, Department of Civil and Resource Engineering, Dalhousie University, Halifax, NS, Canada.

[3] Associate Professor and Canada Research Chair in Sustainable Infrastructure, Department of Civil and Resource Engineering, Dalhousie University, Halifax, NS, Canada.

Abstract

This study examined nine concrete members reinforced with glass fiber-reinforced polymer (GFRP) bars, exploring the impact of combined bending moment and low axial loads. Three reinforcement ratios (1.7, 2.5, and 3.3%) were considered under various axial loads (0, 125, and 250 kN). In the absence of a standardized test method for determining the compressive properties of rebars, a simple approach was adopted. GFRP bars demonstrated a compressive modulus of elasticity that was roughly equivalent to their tensile modulus, along with a compressive strength reaching approximately 70% of their tensile strength. The main tests on members showed that increasing the reinforcement ratio to 3.3% resulted in a 4% reduction in bending resistance with a 2% axial load, while a ratio of 2.5% led to a 7% decrease; conversely, a lower ratio of 1.7% showed a 2% increase in bending resistance under the same load. An analytical model incorporating GFRP bar compression contributions was developed for cross-sectional analysis. It was verified against experimental and literature data, to conduct parametric studies on the impact of reinforcement ratio, concrete strength, GFRP modulus, and strength on the interaction diagram shape under low axial loads. Results demonstrated that there are two major cases of interaction diagram slope in the proximity of the pure moment axis. At higher reinforcement ratios, the moment resistance diminishes at low axial loads when compared to pure moment conditions. However, more research is needed to verify the repeatability of the test results and draw conclusive empirical evidence.

Keywords: GFRP-Reinforced Concrete Members, Low Axial Load, Experimental Investigation, Analytical Model

DOI: https://ascelibrary.org/doi/10.1061/JCCOF2.CCENG-4673

INTRODUCTION

The deterioration of concrete structures in marine environments due to steel reinforcement corrosion poses significant concerns, including reduced strength, increased maintenance costs, compromised performance, and shortened lifespan, as emphasized by a comprehensive assessment of US infrastructure (ASCE 2021) With a substantial portion of the nation's bridges aging and structurally deficient, innovative solutions are urgently needed. Research indicates that fiber-reinforced polymers (FRP), particularly FRP bars, offer a viable replacement for steel reinforcement, addressing corrosion challenges (Alsayed 1998).

In recent years, the latest generation of FRP reinforcing bars, tailored for the construction sector, has become increasingly cost-effective, boasting superior corrosion resistance compared to traditional steel reinforcement. Despite their higher tensile strength, direct substitution with equivalent steel reinforcement poses challenges due to their anisotropic nature from pultrusion manufacturing, along with lower elastic modulus and brittle failure characteristics, necessitating specialized considerations in design codes.

Considerable research has been conducted globally by professional organizations and research institutions, leading to the development and publication of design codes and construction guidelines for structural concrete members reinforced with FRP. Due to the limited availability of experimental research data, the American design guideline ACI PRC-440.1R-15 (ACI 2015) disregarded the contribution of FRP bars in compression. Also, International Federation for Structural Concrete (fib 2007) completely ignored the contribution of GFRP bars in compression due to their anisotropic nature and low contribution in member's capacity. However, based on the results of extensive research in this area, ACI CODE-440.11-22 (ACI 2022) allocated a chapter to the design of GFRP-RC columns. Also, the latest version of the Canadian highway bridge design code CAN/CSA S6-19 (CSA 2019), allows for a design strain limit of 0.002 µm/mm for FRP bars in compression. The Canadian design code CSA S806 (CSA 2021) for building structures with FRP is also revising its limitations to include the design strain limit of 0.002 µm/mm. Some research work in this area is reviewed below. ACI CODE-440.11-22 (ACI 2022) imposes design restrictions on the strains (clause 10.3.2) and, if the factored axial compression, P_u, determined from the analysis of the loads on the column, exceeds $0.1f'_cA_g$, the ultimate tensile strain of the rebars is limited to 1 percent to prevent excessive deformations. This means that lower axial loads are ignored in this limitation.

El-Nemr et al. (2013) investigated the flexural performance of concrete beams reinforced with GFRP bars and found a direct influence of reinforcement ratio on stiffness and deflection. Elgabbas et al. (2016) studied the flexural behavior of concrete beams reinforced with sand coated BFRP bars, emphasizing the role of reinforcement ratio in stiffness and crack width reduction. Ovitigala et al. (2016) observed that increasing the reinforcement ratio in concrete beams reinforced with BFRP bars improved deflection, stiffness, and ultimate moment capacity. El-Nemr et al. (2018) highlighted the importance of gross cross-sectional area and axial reinforcement stiffness in the flexural behavior of concrete beams reinforced with GFRP bars. Abdelkarim et al. (2019) examined the flexural strength and serviceability of concrete beams reinforced with deformed GFRP bars, finding the influence of concrete compressive strength and reinforcement spacing on moment capacity and crack width. Khorramian and Sadeghian (2017) investigated the compressive behavior of concrete columns reinforced with GFRP bars and emphasized the contribution of GFRP bars to compressive strength. Elchalakani et al. (2018) analyzed rectangular columns reinforced with GFRP bars, highlighting the influence of reinforcement ratio and concrete on failure mode and load-deflection behavior. Guerin et al. (2018) studied the effect of reinforcement ratio on axial and flexural strength of concrete columns reinforced with GFRP bars, showing enhanced strength with increased reinforcement ratio. Salah-Eldin et al. (2019) compared the behavior of HSC columns reinforced with GFRP and steel under eccentric axial loads, observing longer post-peak behavior and smaller strength losses in GFRP-reinforced columns. Elchalakani et al. (2020) investigated GFRP-reinforced concrete columns and beams, finding lower load capacities but increased ductility with sufficient transverse reinforcement. Khorramian and Sadeghian (2020) examined concrete columns reinforced with GFRP bars under eccentric compression loading, emphasizing the sustained load, moment, and deformation capacity of GFRP bars after concrete spalling.

The present research aims to investigate the combined effect of bending and low axial loads experimentally and analytically. Three groups of GFRP-reinforced concrete members with varying reinforcement ratios were tested, and their behavior at low axial loads was studied. An analytical model was developed for cross-sectional analysis, incorporating the linear strain relationship within the section, and considering the contribution of GFRP bars in compression. This model was validated using existing data from literature on columns, followed by a comparison with the test results obtained in this study. Furthermore, parametric studies were conducted to study the circumstances under which a low axial load might result in lower moment capacities. The influence of key parameters such as GFRP reinforcement ratio, GFRP modulus, and concrete strength on the shape of the interaction diagram was examined to show the effect of low axial loads for GFRP-reinforced members on their moment capacity.

EXPERIMENTAL PROGRAM

Materials

A ready-mix normal weight concrete was used to make the members, which had a water-to-cement ratio of 0.32, superplasticizers, and retarder, and was made with 12.5 mm maximum aggregate size. The concrete had an average 28-days compressive strength (±standard deviation) of 44.1±1.1 MPa. To determine the average concrete compressive strength, nine cylinders with a diameter of 100 mm and length of 200 mm that were cured under similar conditions were tested on the day of testing in accordance with ASTM C39M (ASTM 2018a).

GFRP bars of #3 and #8 sizes utilized in the study were manufactured through the pultrusion process, comprising glass fibers impregnated in vinyl-ester resin. The manufacturer's (Owens Corning, Toledo, OH, USA) data sheet indicates a fiber content of 80% for these bars. Figure 1 illustrates their cross section, and Table 1 shows the mechanical properties of these bars. Various factors contribute to the disparity in properties between #3 and #8 bars. Larger diameter bars are more prone to inconsistencies in fiber distribution, potentially leading to localized weak points and diminished overall tensile strength. Additionally, their increased surface area may result in slower and less uniform curing during production. Furthermore, larger diameter bars tend to exhibit a higher proportion of fibers oriented parallel to the longitudinal axis, potentially reducing strength compared to smaller diameter bars with a more isotropic fiber distribution.

To determine the ultimate tensile strength (f_{ftu}) and modulus of elasticity (E_{ft}) of the GFRP bars in tension, five coupons were prepared following ASTM D7205M (ASTM 2021b). The tensile stresses were calculated using the applied tensile load divided by the nominal cross-sectional area.

The average peak tensile stress in the stress-strain diagram was used to determine the tensile strength of the bars. The chord modulus of elasticity of the bars in tension was calculated following ASTM 7205M (ASTM 2021b) using the first tensile stress (σ_1) at the strain of 1,000 μm/m and second tensile stress (σ_2) at 3,000 μm/m. The average (±standard deviation) tensile strength and modulus of elasticity of the GFRP bars in tension were 808±14 MPa and 45±0.8 GPa, respectively. The value of the tensile strength was higher than the specified guarantied values by the manufacturer.

A compression test was proposed and conducted on five GFRP bar specimens with a clear length of twice the bar diameter (d_b) and anchored at both ends for a length of four times the diameter, using a length-to-diameter ratio of 2 to determine the ultimate compressive strength (f_{fcu}) and modulus of elasticity (E_{fc}) of the GFRP bars in compression. A suitable method was chosen based on the literature review of previous studies (Fillmore & Sadeghian 2018; Khorramian & Sadeghian 2018). To ensure that there was sufficient material around the GFRP bar to prevent any crushing inside the anchor, a 4-inch diameter pipe size was used, which is larger than the size specified by ASTM 7205M (ASTM 2021b). Figure 2 depicts the specimens' dimensions, preparation method and testing. During compression testing, all specimens exhibited GFRP bar crushing at the gauge length. The compressive behavior observed to be linear, and the strain readings from both sides of the bar were similar, indicating that the load was applied concentrically. The calculation of the chord modulus of elasticity in compression followed the same method as the one used under tension (ASTM 2021b). An average compressive stress of 569±69 MPa from the compressive testing indicated that the GFRP bars could sustain compressive loads of up to 70% of their tensile load. The compressive elasticity modulus was 48±2 GPa, which is slightly higher than the tensile modulus of elasticity and can be attributed to the nonhomogeneous structure of the bars and the behavior of microcracks within the matrix. The stress-strain behavior of the GFRP bars under tension and compression, resulting from tests is illustrated in Figures 3(a) and 3(b), respectively.

Considering the compressive tests on bar specimens, since the pure material properties of the bars are the target, the length-to-diameter ratio of 2 was selected based on ASTM D695-15 (ASTM 2015) to prevent any slenderness effects or buckling. The other studies who considered larger lengths for bars in concrete aimed to study the geometric effects and material properties simultaneously and considered the tie spacing (Jawaheri Zadeh & Nanni 2013), or proposed relationships between the length-to-diameter ratio and the strength (AlAjarmeh et al. 2019; D’Antino & Pisani 2023).

Specimens

Nine prismatic members with rectangular cross-section were designed and tested under various loading conditions, as indicated in Table 2. The cross-section of the members consisted of three layers of longitudinal reinforcement, with one layer as top compression reinforcement and two layers as bottom tension reinforcement. The longitudinal reinforcement was tied together by two C-shaped stirrups at equally spaced intervals of 150 mm center to center at the mid-span and 75 mm center to center at the end span. The spacing between the bottom longitudinal reinforcement was maintained by a spacer bar placed at regular intervals. The specimens were labeled using the convention "B-RX-PY," where "R" indicates the reinforcement ratio, and the following number represents the percentage for that member. "P" denotes the applied axial load, with the subsequent number indicating the percentage of the axial compressive capacity of the member. For instance, "B-R1.7-P4" refers to the members with a 1.7% reinforcement ratio and a 4% axial load capacity. The reinforcement ratio for all members was calculated using:

$$\rho_f = \frac{A_f}{bd} \tag{1}$$

All specimens were of the same dimensions, measuring 330 mm in width, 420 mm in height, and 3050 mm in length, as depicted in Figure 4. The specimens were designed to examine the members' flexural and shear capacity under zero (pure bending), 2.0%, and 4% axial capacity. The members were designed to have an over-reinforced section, with the preferred failure mode being concrete crushing at a maximum compressive strain of 3,000 µm/m, according to ACI CODE-440.11 (ACI 2022).

The specimens were classified into three groups, each with different reinforcement ratios and rebar arrangements at the bottom. The longitudinal reinforcement comprised sand-coated #8 GFRP bars, while #3 GFRP bars were employed for transverse reinforcement.

The cages for the nine specimens were assembled in the Heavy Structure lab at Dalhousie University. C-shaped stirrups were initially assembled for the required outer to outer dimension alignment and then tied using tie-wraps to make a rectangular stirrup. Longitudinal bars were laid between two tables at a distance to support the cage assembly, and the stirrups were inserted from one end and tightened using tie-wraps at midspan and end span of the member with dense stirrups at 75 mm spacing at end span to avoid shear failure. Strain gauges were marked and installed on the longitudinal bars after removing the sand coating layer of GFRP.

Plywood formworks were built for horizontal casting, aiding in uniform vibration during concrete pouring. After smoothing the concrete surface, polythene sheets were applied for protection. Curing began the next day and lasted seven days to retain surface moisture. Figure 5 depicts the preparation process for GFRP reinforced concrete members.

Test Set-up and Instrumentation

The full-scale specimens were subjected to four-point bending with a clear span of 2800 mm, and an overhang of 125 mm on either end. Steel cover plates were used to protect both ends of the specimens to ensure proper confinement and prevent premature failure at the ends or outside the support locations. The test set-up and instrumentation details are provided in Figure 6.

During the testing process, the applied transverse load was increased gradually and the resulting vertical and horizontal displacements, as well as the GFRP strains, were monitored and recorded using the data acquisition system connected to a computer. The transverse load was applied using a 1,000 kN hydraulic actuator with a 5.0 mm/min displacement rate, while the axial load was applied longitudinally to the center of the member's cross-sectional area at one end and was monitored using a load cell. To measure the changes in the compressive and tensile strain of the GFRP reinforcement, a total of four strain gauges were installed on the longitudinal bars. Two strain gauges were installed on the top longitudinal compression bars at the midspan, while two strain gauges were installed on the bottom longitudinal bars under tension at the midspan. Linear Potentiometer (LPs) were used to measure the vertical displacement at the quarter, midspan, and three-quarter of the span, and for horizontal displacement at one end of the member. A Strain Pot (SP) was used at mid-span to check the LP readings.

Results and Discussion

This section analyzes the experimental results of the test specimens, including failure modes, load-deformation, load-strain, moment-curvature, and axial load-moment behavior. Table 3 presents the ultimate moment capacity of the specimens, along with their corresponding ultimate concrete strain, tensile strain, quarter-span, and mid-span deflections. The listed moment values were calculated based on transverse load data multiplied by shear span and vertical deflection, with axial load applied longitudinally to the specimens tested with 2% and 4%.

All nine test specimens exhibited a similar failure pattern, characterized by the initial formation of vertical cracks in the constant moment region at midspan perpendicular to the longitudinal reinforcement, followed by the widening of flexural cracks and the development of flexural-shear cracks which started vertical and continued diagonal at shear span with increasing loading. Cracks were more prevalent in the lower reinforcement ratio members. The members sustained higher loads until the concrete in the top compression zone cracked and crushed at the ultimate limit of maximum strain.

Load – Deflection Behavior and Failure Modes

Deflection was captured at both quarter spans and mid-span. Load-deflection curves, from transverse loads and the average deflection of the two LPs, for all reinforcement ratios at different axial loads of 0, 125, and 250 kN were plotted. The deflection of all specimens before cracking was minimal, with a sudden increase after post-cracking. A sudden drop was observed in transverse load causing a decrease in deflection at concrete crushing, which gradually increased as GFRP bars actively sustained the applied load until failure by shear or flexure (Figure 7).

Fig. 8 illustrates the load–deflection curves, revealing a relationship between the reinforcement ratio and members’ deflection behavior. Notably, an increase in member’s stiffness correlates with a reduction in deflection. As seen, by increasing the reinforcement ratio, the slope of the load–deflection curve increased. This figure also provides insights into various failure modes observed during the experimentation. Predominantly, failures originated from CC around a deflection of 40 mm, and subsequently transitioned into SF. However, Fig. 8(a) presents a scenario where shear failure was delayed, an FF occurred at the highest axial load (250 kN), and the lowest reinforcement ratio resulted in a greater deflection of approximately 95 mm. Conversely, the other two specimens subjected to axial loads of 0 and 125 kN experienced concrete crushing and shear failure at comparatively lower strains. It can be inferred that if SF did not occur for the other two members (subjected to 0 and 125 kN axial load), they would have exhibited similar behavior up to FF. Moving to Fig. 8(b), members with an average reinforcement ratio (2.5%) predominantly exhibited concrete crushing, leading to shear failure. However, Fig. 8(c) presents a case where specimens experienced shear failure after concrete crushing. Shear indeed is a complicated phenomenon and in the curve corresponding to P = 125 kN shown in Fig. 8(c) it appears to have occurred way after the concrete crushing, which resulted in higher deflections in the member. Additionally, it is worth noting that the specimen subjected to a 125 kN axial load displayed higher deflections due to delayed SF. These observations highlight the need for increased shear reinforcement to effectively delay shear failure. Furthermore, it suggests that further testing is necessary in the future to gain a deeper understanding of the effects of low axial loads, given the insights gleaned from these experiments.

Load – Strain Behavior

Strain gauges were mounted to monitor the compressive and tensile strains of the bars, and registered consistent readings throughout the testing process. The transverse load-strain diagram in Figure 9 shows a linear-elastic behavior for both tensile and compressive bars. Strains in tensile bars went up to around 13,000 μm/m for most of the strain gauges, and in one case, test specimen B-R1.7-P4 experienced the highest tensile strain of 18,000 μm/m in GFRP. The compressive bars' strains showed a linear behavior up to the crushing point of concrete (3,000 μm/m) and after that the failure of concrete affected the strain gauge readings.

Tensile strain readings showed a decrease as reinforcement ratio increased from 1.7 to 3.3%, with the 1.7% specimen exhibiting a sharp increase. The impact of axial load was minimal, but noticeable in the tensile strain curve. GFRP bars remained well below their ultimate strain until the first peak load, at which point a load drop of 6-8% occurred. Further increase in transverse load caused the GFRP bars to reach their ultimate strain at the second peak load, resulting in shear failure of the concrete and GFRP rupture at the top longitudinal bar.

All specimens in this study past the strain of 3,000 μm/m, representing the point of concrete crushing, which was the primary focus of our investigation. At this juncture of concrete crushing, the transverse loads were extracted, and their corresponding moments were calculated.

Moment – Curvature Behavior

Figure 10 depicts the moment-curvature response. Curvature was determined using the difference in average experimental tensile and compressive strain of GFRP bars divided by the difference in depth, *d*, of the strain gauge location:

$$\psi_m = \frac{\varepsilon_{ft} - \varepsilon_{fc}}{s_d} \tag{2}$$

In which ψ_m is the curvature at mid-span (1/mm), ε_{ft} is the average tensile strain in bottom GFRP bar (μm/m), ε_{fc} is the average compressive strain in top GFRP bar (μm/m), and s_d is the distance between the strain gauges in the top and bottom reinforcement (mm). The moment-curvature behavior exhibited linear characteristics, similar to those observed in FRP strain behavior. The first peak load observed when concrete crushing happened for all tested specimens, followed by linear behavior until failure due to flexure or shear at the second peak load.

The GFRP specimen reached its ultimate bending resistance due to the contribution of GFRP bars to the member's bending resistance, which increased gradually as the compressive strain in the bars grew. The highest curvature was 61.2×10^6 1/mm from specimen B-R1.7-P4, which failed in flexural and experienced higher deflection before concrete crushing (Figure 10(a), green curve). The lowest curvature was 28.5×10^6 1/mm from specimen B-R3.3-P4, which failed abruptly in shear (Figure 10(c), green curve).

ANALYTICAL STUDIES

The analytical model is developed to conduct a cross-sectional analysis by considering the contribution of GFRP bars in compression, which is often overlooked in current design codes. It was observed (Khorramian & Sadeghian 2020) that compression bars contribute to load-bearing both before and after concrete crushing, leading to increased compressive strength and moment resistance in members. Below, the specifications and the underlying hypothesis of the model are presented.

Model Description

The analytical model was developed to perform multiple cross-sectional analyses aimed at generating the P-M interaction diagram. This involved adjusting the depth of the neutral axis, denoted as 'c', and computing the forces and moments in both the concrete and bars for that specific neutral axis depth.

To find the force in concrete, the cross-section was discretized into 20 concrete fibers of equal thickness and concrete stress was calculated based on the values from stress-strain curve of concrete at the center of each fiber. The concrete behavior in compression was determined using equations derived from Popovics (1973) and Thorenfeldt et al. (1987). The latter considered a curve fitting factor to precisely predict the descending part of the stress-strain curve. The modulus of elasticity of concrete, $E_c = 4700\sqrt{f_c'}$, was determined following ACI 318-19 (ACI 2019). Only compressive stresses in concrete were considered with an ultimate compressive strain of 3,000 μm/m, and the tensile stress in concrete was ignored completely. It was assumed that full composite action existed between the concrete and GFRP, resulting in a linear strain profile throughout the section from the top-end compressive face to the bottom end tensile face of the member. The strain at each segment of concrete fiber was determined, and the corresponding stresses were calculated at each segment. Figure 11 illustrates the strain profile and parabolic stress diagram with appropriate symbols.

Linear stress-strain relationship was assumed for GFRP bars with an ultimate tensile strength, f_{ftu}, of 808 MPa, and an ultimate compressive strength, f_{fcu}, of 568 MPa. The analysis considered the GFRP bar's full contribution in compression, and a modulus of elasticity of 46 GPa was assumed for both tensile and compressive reinforcements. The axial compression or tension force in the GFRP bar was determined based on the modulus of elasticity and the area of GFRP bars. All φ factors for the compression and tension-controlled part of this member section were considered to be unity. The total compressive forces in each concrete fiber above the neutral axis were calculated, considering the section's width and thickness of each segment, and concrete stress at the location of compressive bars was deducted:

$$C_c = \sum_{j=1}^{20} f_{cj}\, b\, \Delta y - \sum_{i=1}^{3} f_{ci}\, A_{fi} \tag{3}$$

The total compressive force is the summation of the forces from each concrete fiber and the compressive bars minus the forces in tensile bars:

$$P_n = C_c + \sum_{i=1}^{3} F_{fci} - \sum_{i=1}^{3} F_{fti} \tag{4}$$

The bending moment due to axial forces in the GFRP bars (M_f) and concrete fibers above the neutral axis (M_c) was computed by considering the lever arm from the neutral axis (y):

$$M_f = \sum_{i=1}^{3} F_{fi}\; y_i \tag{5}$$

$$M_c = \sum_{j=1}^{20} f_{cj}\, b\, \Delta y\, y_j - \sum_{i=1}^{3} f_{ci}\, A_{fi} y_i \tag{6}$$

The total bending moment (M_n) of the member section is the summation of bending moment due to the forces in concrete fibers (M_c), and the moment due to the axial force in GFRP bars (M_f). The total compressive force (P_n), and the corresponding bending moment (M_u) of the member were calculated to form the *P*-*M* interaction diagram:

$$e_{N.A} = \frac{M_n}{P_n} \tag{7}$$

$$M_c = P_n e, \;\; e = e_{N.A} + c_p - c \tag{8}$$

Wherein, $e_{N.A}$ is the load eccentricity from the neutral axis, while e is the eccentricity from section's center of plastic, c_p.

Model Verifications

The developed analytical model is verified against four experimental and analytical studies to investigate the effect of reinforcement ratio, concrete strength, selection of concrete stress-strain model, etc. on strength and stiffness in normal concrete and high strength concrete columns reinforced with GFRP bars.

In the first study by Khorramian & Sadeghian (2017), nine specimens of dimensions 150×150×500 mm were tested with varying eccentricity-to-width ratios (0.1, 0.2, and 0.3), and interaction diagrams based on Popovics (1973) and Thorenfeldt (1987) stress-strain models were presented alongside test outcomes in Figure 12(a), highlighting the risk of neglecting accidental axial load at the maximum ultimate moment of GFRP beams. The second validation, based on the study by Salah-Eldin et al (2019), utilized beam sections of dimensions 400×400×2000 mm and concrete strength of 71.2 MPa, with BFRP tensile strength at 1646 MPa, showcasing good agreement between the Thorenfeldt (1987) model and experimental data for high-strength concrete in Figure 12(b). The subsequent verification analysis by Khorramian & Sadeghian (2020) involved short and slender concrete columns, reinforced with #6 GFRP bars, with two reinforcement ratios

(2.78% and 4.80%) and a compressive strength of 48.4 MPa, demonstrating reasonable agreement between the Popovics (1973) model and experimental results, as shown in Figure 12(c) and (d). Lastly, the verification analysis with the study by Salah-Eldin et al. (2020) involved high-strength GFRP reinforced concrete columns of dimensions 400×400×2,000 mm with varying GFRP reinforcement ratios (0.5%, 1.0%, and 2.5%) and an average concrete compressive strength of 71.2 MPa, indicating agreement between the analytical model and experimental results, as depicted in Figure 12(e) and (f).

Figure 13 compares the analytical model of this study with the test outputs on GFRP reinforced concrete members on the *P-M* interaction diagram. The axial load and bending moment values at concrete failure (ε_{cu}=3,000 µm/m) were calculated and reported in Table 4. At a higher reinforcement ratio of 3.3%, experiments showed that the bending resistance of 323 kN-m at zero axial load decreased to 311 kN-m when a low axial load of 2% was induced in the member. For a reinforcement ratio of 2.5%, the bending resistance of 303 kN-m at zero axial load decreased to 283 kN-m with 2% axial load. In contrast, for a lower reinforcement ratio of 1.7%, the pattern was opposite, with the bending resistance of 250 kN-m at zero axial load increasing to 273 kN-m with the application of a low axial load of 2%. It was observed that applying a low axial load at a higher reinforcement ratio resulted in a greater reduction in the bending resistance of the member compared to the lower reinforcement ratio. However, increasing the low axial load to 4% increased the bending resistance of the member even at higher reinforcement ratios. Looking at the trend of the bending moments versus the axial load illustrates that increasing the low axial load in GFRP-reinforced members does not always increase the bending moment (as seen for 2% axial load). This difference between the behavior of such members with the steel-reinforced ones should be considered in practical applications. Possible sources of difference between test results and analytical model include movement of the testing frame, variation in center-to-center member support locations, variation in shape and dimension of stirrups, axial load eccentricity.

A comparison is made between the experiments outcomes and the interaction diagram based on ACI CODE-440.11-22 (ACI 2022). Two different curves can be seen in Figure 14. The curve corresponding to nominal values was generated using equivalent concrete stress block. Concrete stress of $0.85f'_c$ is assumed uniformly distributed over an equivalent rectangular area with the stress block factor, β_1, which is considered ranging from 0.65 to 0.85 as a function of concrete compressive strength. The design curve uses the strength reduction factor, ϕ, ranges from 0.55 to 0.65 for concrete under combined moment and axial force (ACI, 2022). As observed, the code's predictions align well with the test results. The interaction diagram generally indicates lower moment capacities, except for one instance where the test result falls below the predicted value, specifically for the minimum reinforcement ratio. Nonetheless, considering the ϕ factor in the design eliminates uncertainties, ensuring a safe design.

Parametric Studies

This section describes the parametric studies conducted using the analytical model, aiming to examine the impact of low axial loads. It focuses on analyzing the shape of the interaction diagram near the bending moment axis across various reinforcement ratios and concrete strengths. Parametric studies consist of two parts. In the first part, it was investigated that under what conditions it is needed to pay special attention to the low axial force. Figure 15 illustrates the interaction diagrams for an example beam-column of 400×400 mm cross section, with f'_c=40 MPa, and different reinforcement ratios of 0.5, 1, 2, 3, and 4%. The location of the balance point, which is a point on the interaction diagram where both concrete and tensile bars fail simultaneously, is contingent on the reinforcement ratio. Notably, for the minimal reinforcement ratio (ρ=0.5%), the balance point resides on the compression side of the diagram. Conversely, for other ratios, it is situated on the tensile side. A distinguishing factor between steel-reinforced and FRP-reinforced beam-columns is evident in the balance point's location. In steel-reinforced cases, the balance point aligns with the belly of the diagram on the compression side, attributed to the yielding point of steel being significantly less than the ultimate strength of FRP bars. This behavior is approximated as bilinear for steel, while FRP bars exhibit linear behavior until the point of failure. Additionally, the figure illustrates a low axial load equivalent to $0.1f'_cA_g$ as per ACI (ACI 2022). It is evident that as the reinforcement ratio increases, the impact of the low axial load becomes more pronounced.

The second part of parametric studies was conducted to shed additional light on the circumstances under which a low axial load might result in lower moment capacities, akin to the highest reinforcement ratio depicted in Figure 15. The influence of the reinforcement ratio, concrete strength, and GFRP modulus on the behavior of GFRP-reinforced beam-column sections was scrutinized through an examination and comparison of the *P-M* interaction diagrams. The studies encompassed reinforcement ratios ranging from 2% to 4%, along with concrete strengths ranging from 20 to 60 MPa. The rebars exhibited elasticity moduli and strengths (both tensile and compressive) within the ranges of 40-60 GPa and 800-1200 MPa, respectively. Consequently, a total of 27 combinations of material properties were investigated for each reinforcement ratio, amounting to a total of 81 analyses across the three reinforcement ratios. The selection of parameter ranges was made within typical material property ranges. While certain combinations, like using 3.3% reinforcement for concrete with f'_c=20 MPa, may seem improbable, the objective of the parametric studies was to observe overarching trends.

Figure 16 presents the outcomes of these parametric studies. As seen, the configuration of the diagram is directly dependent on both the concrete strength and the elasticity modulus of the rebars. Increasing the concrete strength for each reinforcement ratio leads to concurrent increases in moment capacity and axial load-bearing capacity, thereby causing a shift in the slope of the diagram near the pure moment axis. An increase in concrete strength, while maintaining a constant value for the rebar elasticity modulus, mitigates the negativity of the slope, resulting in a less moment resistance at low axial loads. Conversely, for relatively lower concrete strengths, the contribution of the rebars assumes greater significance, causing the diagrams to exhibit more negative slopes. This phenomenon is particularly pronounced in cases of the lowest concrete strength, wherein the low axial load shows a relatively greater effect on the moment capacity of the member. Moreover, this effect becomes more noticeable with increasing reinforcement ratios. It is important to note that variations in material strengths have no noticeable impact on the positive side of the diagram, which constitutes the focal point of this study, as the balance point of GFRP-reinforced concrete beam-columns resides on the negative axial load side.

ACI CODE-440.11-22 (ACI, 2022) stipulates in clause R9.5.2.2 that “Beams resisting significant axial forces (higher than $0.1f'_cA_g$) require consideration of the combined effects of axial forces and moments”. This identical provision can be found in the same clause within ACI 318-19 (ACI, 2019) designed for steel-reinforced concrete. Consequently, it implies that the code treats both GFRP-reinforced and steel-reinforced concrete members uniformly, focusing solely on the impact of axial loads when they reach a significant level. Nevertheless, this study introduced the concept that low axial loads may reduce the moment-carrying capacity of the members. While this effect may not be substantial, it is recommended to consider its implications, especially when the reinforcement ratio and the elasticity modulus of the bars are relatively high.

It should be noted that the findings of this study are limited to single beams, and the influence of the slab has not been considered. The slab-beam system has higher stiffness which affects the moment capacity of the beam.

CONCLUSIONS

In this research, a total of nine concrete beams reinforced with GFRP bars measuring 330×430 mm in cross-sectional shape and 3100 mm length were investigated both experimentally and analytically to study the effect of combined bending moment and low axial loads. All specimens were divided into three groups of reinforcement ratio 1.7%, 2.5%, and 3.3% and tested under four-point bending under varying axial load of zero, 125 kN, and 250 kN. The analytical model was developed to be verified against the experimental results and be used for parametric studies on different contributing parameters. Based on the presented results and comparison, the following conclusions were drawn:

- Unlike steel-reinforced concrete members, low axial loads (less than 10% of the axial capacity) may reduce ultimate bending resistance, particularly at higher reinforcement ratios in GFRP-reinforced members. According to the experiments, a decrease in moment resistance of up to 7% was observed with the application of an axial load equivalent to 2% of the axial capacity. Nonetheless, considering the ϕ factor in the ACI design code eliminates some uncertainties.
- The proposed coupon compression test demonstrated that the compressive strength of the bars averaged 70% of their tensile strength. Additionally, the modulus of elasticity of GFRP bars was found to be approximately equivalent to their tensile modulus of elasticity, albeit negligibly higher in compression.
- Beams with higher reinforcement ratios showed decreased deflection due to their higher

stiffness. GFRP bars remained below ultimate strain until the first peak load, followed by a 6-8% load drop. Further transverse loading led to their ultimate strain at the second peak, causing SF/FF and GFRP rupture. Moment-curvature behavior resembled FRP strain, with CC at the first peak load, followed by SF/FF at the second. Higher shear reinforcement delays SF and increases the probability of observing FF as the failure mode.

- The analytical model developed in this study offers an approach to cross-sectional analysis, considering the contribution of GFRP bars in compression. Model verifications against experimental and analytical studies showcased its reliability across various reinforcement ratios and concrete strengths, demonstrating reasonable agreement with test outcomes.
- Parametric studies using the analytical model, which was verified against the experimental data, further investigated the behavior of GFRP-reinforced concrete beam-columns at low axial loads, considering reinforcement ratio, concrete strength, GFRP modulus and strength. Results demonstrated steeper negative slopes in the proximity of the pure moment axis in the interaction diagram for higher elasticity modulus of rebars. Under these circumstances, neglecting the low axial load may not be toward a conservative design.
- Due to uncertainties in the tests, including factors such as concrete strength, FRP properties, maintaining axial load, and potential frame movements, the observed variations in the bending moment resistance of the specimens do not conclusively suggest that ignoring low axial loads leads to an unsafe design. Results of this study showed the concept of low-axial load; however, more research is needed to verify the repeatability of the test results and reach a definitive conclusion.
- Based on the limitation of this study, exploring T-shaped beams for future research due to the stiffness enhancement from the slab in a slab-beam system is suggested. Furthermore,

it is recommended to incorporate substantial shear reinforcement to facilitate the observation of concrete behavior at higher strains and to delay shear failure.

DATA AVAILABILITY STATEMENT

The data or code that support the findings of this study are available from the corresponding author upon reasonable request.

NOTATION

The following symbols are used in this paper:

A_f = Longitudinal reinforcement total cross-sectional area, mm^2

A_g = Beam-column cross-sectional area, mm^2

b = Width of beam-column cross-section, mm

c = Neutral axis of the section, mm

C_c = Total concrete compressive force of beam section, kN

c_p = Center of plastic of the section, mm

d = Beam-column effective depth, mm

d_i = Depth of each reinforcement layer, mm

e = Eccentricity from section’s center of plastic, mm

E_c = Modulus of elasticity of concrete, MPa

E_f = Modulus of elasticity of GFRP, MPa

E_{fc} = Modulus of elasticity of GFRP in compression, MPa

E_{ft} = Modulus of elasticity of GFRP in tension, MPa

$e_{N.A}$ = Load eccentricity from the neutral axis, mm

f'_c = Concrete compressive strength, MPa

f_{cj} = Concrete stress corresponding to axial strain of concrete fiber, MPa

f_{cr} = Cracking strength of concrete, MPa

f_{fcu} = Compressive strength of GFRP bars, MPa

f_{fi} = Axial stress of GFRP, MPa

f_{ftu} = Tensile strength of GFRP bars, MPa

h = Height of beam-column cross-section, mm

M_c = Total bending moment due to axial force in concrete fiber, kN-m

M_f = Total bending moment due to axial forces in the GFRP bars, kN-m

M_n = Total bending moment, kN-m

n_f = Ratio of modulus of elasticity of FRP bars to modulus of elasticity of concrete (-)

P_n = Total compressive force of beam-column section, kN

s_d = Distance between the strain gauges in the top and bottom reinforcement, mm

y = distance from neutral axis in cross-sectional analysis, mm

β_1 = Factor for equivalent stress block depth, (-)

Δ_y = Thickness of concrete segment, mm

ε_{cu} = Ultimate concrete strain, µm/m

ε_{fc} = Average compressive strain of top GFRP bar in the section, µm/m

ε_{ft} = Average tensile strain of bottom GFRP bar in the section, µm/m

ρ_f = FRP reinforcement ratio, (-)

φ = Resistance factor, (-)

ψ_m = Curvature of the beam-column at mid-span, m^{-1}

REFERENCES

Abdelkarim, O. I., Ahmed, E. A., Mohamed, H. M., & Benmokrane, B. (2019). Flexural strength and serviceability evaluation of concrete beams reinforced with deformed GFRP bars. *Engineering Structures*, *186*, 282–296.

ACI. (2015). *ACI PRC-440.1R-15: Guide for the Design and Construction of Structural Concrete Reinforced with FRP Bars*. American Concrete Institute.

ACI. (2019). *ACI 318-19: Building Code Requirements for Structural Concrete and Commentary*. American Concrete Institute.

ACI. (2022). *ACI CODE-440.11-22: Building Code Requirements for Structural Concrete Reinforced with Glass Fiber-Reinforced Polymer (GFRP) Bars-Code and Commentary*. American Concrete Institute.

AlAjarmeh, O. S., Manalo, A. C., Benmokrane, B., Vijay, P. V, Ferdous, W., & Mendis, P. (2019). Novel testing and characterization of GFRP bars in compression. *Construction and Building Materials*, *225*, 1112–1126.

Alsayed, S. H. (1998). Flexural behaviour of concrete beams reinforced with GFRP bars. *Cement and Concrete Composites*, *20*(1), 1–11. https://doi.org/https://doi.org/10.1016/S0958-9465(97)00061-9

ASCE. (2021). *A comprehensive assessment of America's infrastructure*. American Society of Civil Engineers.

ASTM. (2015). *ASTM D695 − 15, Standard Test Method for Compressive Properties of Rigid Plastics*. American Society for Testing and Materials.

ASTM. (2018). *ASTM C39 / C39M, Standard Test Method for Compressive Strength of Cylindrical Concrete Specimens*.

ASTM. (2021). *ASTM D7205/D7205M, Standard Test Method for Tensile Properties of Fiber-Reinforced Polymer Matrix Composite Bars*.

CSA. (2019). *S6:19 - Canadian Highway Bridge Design Code applies to the design*. Canadian Standards Association.

CSA. (2021). *S806:12(R21) - Design and construction of building structures with fibre-reinforced polymers*. Canadian Standards Association.

D'Antino, T., & Pisani, M. A. (2023). Tensile and compressive behavior of thermoset and thermoplastic GFRP bars. *Construction and Building Materials*, *366*, 130104.

Elchalakani, M., Dong, M., Karrech, A., Mohamed Ali, M. S., & Huo, J.-S. (2020). Circular concrete columns and beams reinforced with GFRP bars and spirals under axial, eccentric, and flexural loading. *Journal of Composites for Construction*, *24*(3), 04020008.

Elchalakani, M., Karrech, A., Dong, M., Ali, M. S. M., & Yang, B. (2018). Experiments and finite element analysis of GFRP reinforced geopolymer concrete rectangular columns subjected to concentric and eccentric axial loading. *Structures*, *14*, 273–289.

Elgabbas, F., Vincent, P., Ahmed, E. A., & Benmokrane, B. (2016). Experimental testing of basalt-fiber-reinforced polymer bars in concrete beams. *Composites Part B: Engineering*, *91*, 205–218.

El-Nemr, A., Ahmed, E. A., & Benmokrane, B. (2013). Flexural Behavior and Serviceability of Normal- and High-Strength Concrete Beams Reinforced with Glass Fiber-Reinforced Polymer Bars. *ACI Structural Journal*, *110*(6).

El-Nemr, A., Ahmed, E. A., El-Safty, A., & Benmokrane, B. (2018). Evaluation of the flexural strength and serviceability of concrete beams reinforced with different types of GFRP bars. *Engineering Structures*, *173*, 606–619.

Fillmore, B., & Sadeghian, P. (2018). Contribution of longitudinal glass fiber-reinforced polymer bars in concrete cylinders under axial compression. *Canadian Journal of Civil Engineering*, *45*(6), 458–468.

Guérin, M., Mohamed, H. M., Benmokrane, B., Shield, C. K., & Nanni, A. (2018). Effect of Glass Fiber-Reinforced Polymer Reinforcement Ratio on Axial-Flexural Strength of Reinforced Concrete Columns. *ACI Structural Journal*, *115*(4).

International Federation for Structural Concrete (fib). (2007). *FRP reinforcement in RC structures - Bulletin 40*. fib.

Jawaheri Zadeh, H., & Nanni, A. (2013). Design of RC columns using glass FRP reinforcement. *Journal of Composites for Construction*, *17*(3), 294–304.

Khorramian, K., & Sadeghian, P. (2017). Experimental and analytical behavior of short concrete columns reinforced with GFRP bars under eccentric loading. *Engineering Structures*, *151*, 761–773. https://doi.org/https://doi.org/10.1016/j.engstruct.2017.08.064

Khorramian, K., & Sadeghian, P. (2018). New testing method of GFRP bars in compression. *CSCE Annual Conference 2018, Fredericton, NB, Canada*.

Khorramian, K., & Sadeghian, P. (2020). Experimental investigation of short and slender rectangular concrete columns reinforced with GFRP bars under eccentric axial loads. *Journal of Composites for Construction*, *24*(6), 04020072.

Ovitigala, T., Ibrahim, M. A., & Issa, M. A. (2016). Serviceability and Ultimate Load Behavior of Concrete Beams Reinforced with Basalt Fiber-Reinforced Polymer Bars. *ACI Structural Journal*, *113*(4).

Popovics, S. (1973). A numerical approach to the complete stress-strain curve of concrete. *Cement and Concrete Research*, *3*(5), 583–599.

Salah-Eldin, A., Mohamed, H. M., & Benmokrane, B. (2019). Structural performance of high-strength-concrete columns reinforced with GFRP bars and ties subjected to eccentric loads. *Engineering Structures*, *185*, 286–300. https://doi.org/https://doi.org/10.1016/j.engstruct.2019.01.143

Salah-Eldin, A., Mohamed, H. M., & Benmokrane, B. (2020). Effect of GFRP reinforcement ratio on the strength and effective stiffness of high-strength concrete columns: Experimental and analytical study. *Journal of Composites for Construction*, *24*(5), 04020055.

Thorenfeldt, E. (1987). “Mechanical properties of high-strength concrete and applications in design.” *In Proc., Symp. Utilization of High-Strength Concrete. Trondheim, Norway: Tapir.*

Table 1. Properties of GFRP bars as per the manufacturer Owens Corning (Toledo, OH, USA)

Bar Size	Nominal Diameter (mm)	Nominal Area (mm^2)	Ultimate Tensile Strength (MPa)	Tensile Modulus (GPa)	Ultimate Strain (%)
#3	10	71.3	827	46	1.79%
#8	25	506.7	620	46	1.34%

Table 2. Test matrix

Specimen Number	Beam ID	Beam Type	Axial Load (%)	Axial Load (kN)	Longitudinal Bars Size	Longitudinal Bars No. of Bars	GFRP Ratio %
1	B-R1.7-P0	1	0	0	#8	6	1.7
2	B-R1.7-P2	1	2	125	#8	6	1.7
3	B-R1.7-P4	1	4	250	#8	6	1.7
4	B-R2.5-P0	2	0	0	#8	8	2.5
5	B-R2.5-P2	2	2	125	#8	8	2.5
6	B-R2.5-P4	2	4	250	#8	8	2.5
7	B-R3.3-P0	3	0	0	#8	10	3.3
8	B-R3.3-P2	3	2	125	#8	10	3.3
9	B-R3.3-P4	3	4	250	#8	10	3.3

Table 3. Test results summary

Sl. No.	Specimen ID	Reinforcement Ratio (%)	Axial Load (kN)	Peak Load (kN)	M_u (kN-m)	Mid-span Vertical Deflection (mm)	Mode of Failure
1	B-R1.7-P0	1.7	0	454.0	248.7	33.8	CC*→SF
2	B-R1.7-P2	1.7	125	488.0	268.4	37.2	CC→SF
3	B-R1.7-P4	1.7	250	498.3	274.1	34.7	CC→FC
4	B-R2.5-P0	2.5	0	550.6	302.8	33.3	CC→SF
5	B-R2.5-P2	2.5	125	508.4	279.6	27.2	CC→SF
6	B-R2.5-P4	2.5	250	555.7	305.7	31.0	CC→SF
7	B-R3.3-P0	3.3	0	587.2	323.0	26.9	CC→SF
8	B-R3.3-P2	3.3	125	559.1	307.5	26.1	CC→SF
9	B-R3.3-P4	3.3	250	641.9	353.1	28.3	CC*→SF

SF: Shear Failure
CC: Concrete Crushing
FC: FRP Crushing
* Concrete crushing was not visible during the test, but the extrapolated value of concrete strain reached 3,000 μm/m

Table 4. Axial load and bending moment values from the tests at concrete failure

Beam-Column	Reinforcement ratio, ρ	P' (kN)	P (@ε_{cu}=0.003) (kN)	Deflection (Δ) (mm)	$M_0=(P/2)\times a$ * (kN-m)	$M'=P'\times\Delta$ (kN-m)	$M=M_0+M'$ (kN-m)
Type_1	1.7%	0	454.0	33.8	249.7	0.0	249.7
		125	487.3	37.1	268.0	4.6	272.6
		250	497.9	34.6	273.8	8.7	282.5
Type_2	2.5%	0	550.5	33.3	302.8	0.0	302.8
		125	508.3	27.2	279.6	3.4	283.0
		250	555.4	30.9	305.4	7.7	313.2
Type_3	3.3%	0	587.2	26.9	322.9	0.0	322.9
		125	559.0	25.9	307.4	3.2	310.7
		250	641.9	40.8	353.0	10.2	363.2

*a: The shear span equal to 1100 mm

List of figure captions

Figure 1. Cross section view of the rebars

Figure 2. GFRP compression test set-up: (a) schematic (b) fabrication (c) all fabricated specimens (d) during testing (e) failure

Figure 3. The stress-strain response of the tested GFRP bars in a) Tension and b) Compression

Figure 4. Beam dimensions and reinforcement details (dimension in mm)

Figure 5. GFRP-reinforced concrete beam fabrication

Figure 6. GFRP-reinforced concrete beam test set-up and instrumentation details (a) schematic (b) actual (all dimensions are in mm)

Figure 7. Failure Pattern – Beams with 1.7% Reinforcement Ratio (Note: CC is Concrete Crushing, SF is Shear Failure, and FF is Flexural Failure.)

Figure 8. Load vs deflection curve at mid-span (a) $\rho = 1.7\%$ (b) $\rho = 2.5\%$ (c) $\rho = 3.3\%$ (Note: CC is Concrete Crushing, SF is Shear Failure, and FF is Flexural Failure.)

Figure 9. Load vs GFRP strain at mid-span (a) $\rho = 1.7\%$ (b) $\rho = 2.5\%$ (c) $\rho = 3.3\%$; Note: All the strains are in μm/m

Figure 10. Load vs extreme concrete strain (extrapolated) at mid-span (a) $\rho = 1.7\%$ (b) $\rho = 2.5\%$ (c) $\rho = 3.3\%$; Note: Strains at concrete are not direct measurements and are extrapolated based on the FRP bar strains

Figure 11. Moment vs Curvature at mid-span (a) $\rho = 1.7\%$ (b) $\rho = 2.5\%$ (c) $\rho = 3.3\%$

Figure 12. Stress and strain profile of GFRP-reinforced concrete beam cross-section

Figure 13. Comparing beam-column interaction diagram from analytical model and the test data by: a) (Khorramian & Sadeghian, 2017), b) (Salah-Eldin et al., 2019), c and d) (Khorramian & Sadeghian, 2020), e and f) Salah-Eldin et al. (2020)

Figure 14. Axial load vs moment (a) $\rho = 1.7\%$ (b) $\rho = 2.5\%$ (c) $\rho = 3.3\%$ (analytical and experimental comparison)

Figure 15. Test data versus interaction diagrams based on equivalent stress block according to ACI-Code 440.11-22 (ACI, 2022): a) $\rho=1.7\%$, b) $\rho=2.5\%$, c) $\rho=3.3\%$

Figure 16. Illustration of different types of interaction diagrams for various reinforcement ratios in an example FRP-reinforced concrete beam-column

Figure 17. Interaction diagrams of the beam-column in this study with various material properties for concrete and rebars for parametric studies: reinforcement ratios of a) 1.7%, b) 2.5%, and c) 3.3%

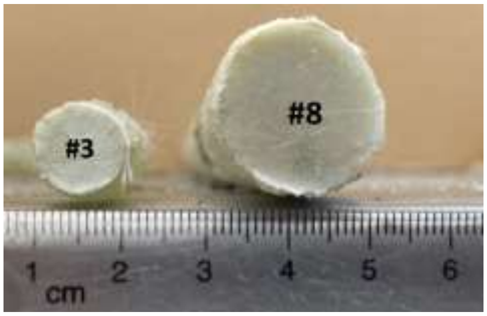

Figure 1. Cross section view of the rebars

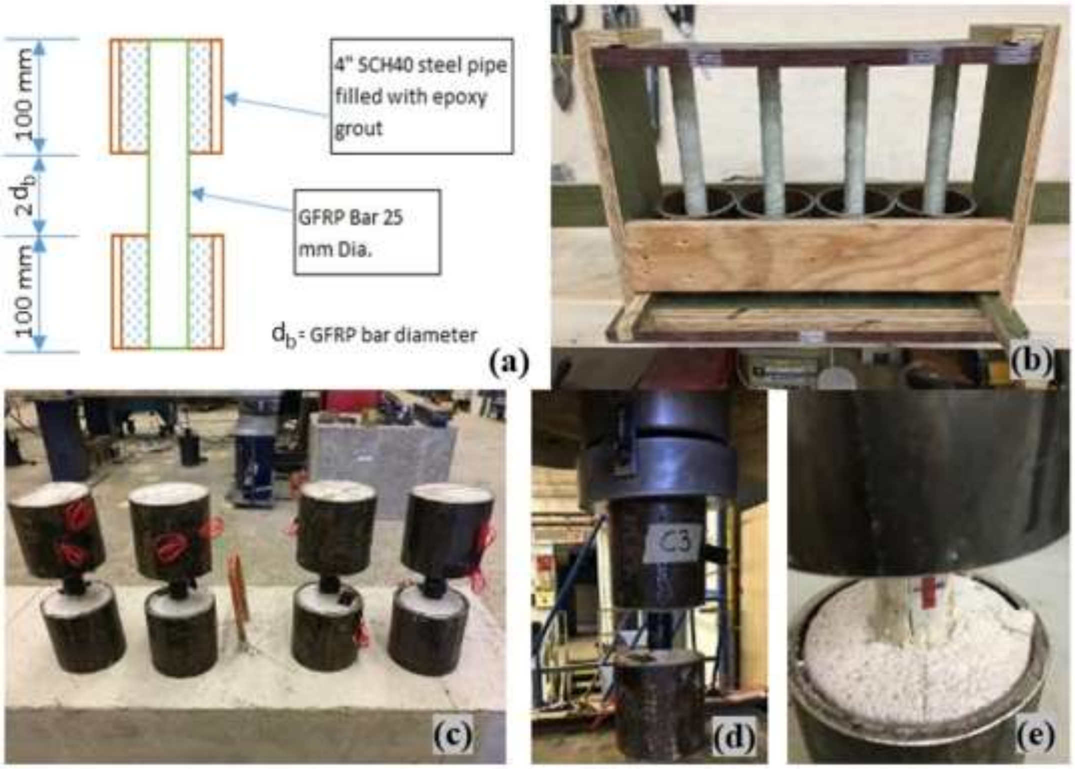

Figure 2. GFRP compression test set-up: (a) schematic (b) fabrication (c) all fabricated specimens (d) during testing (e) failure

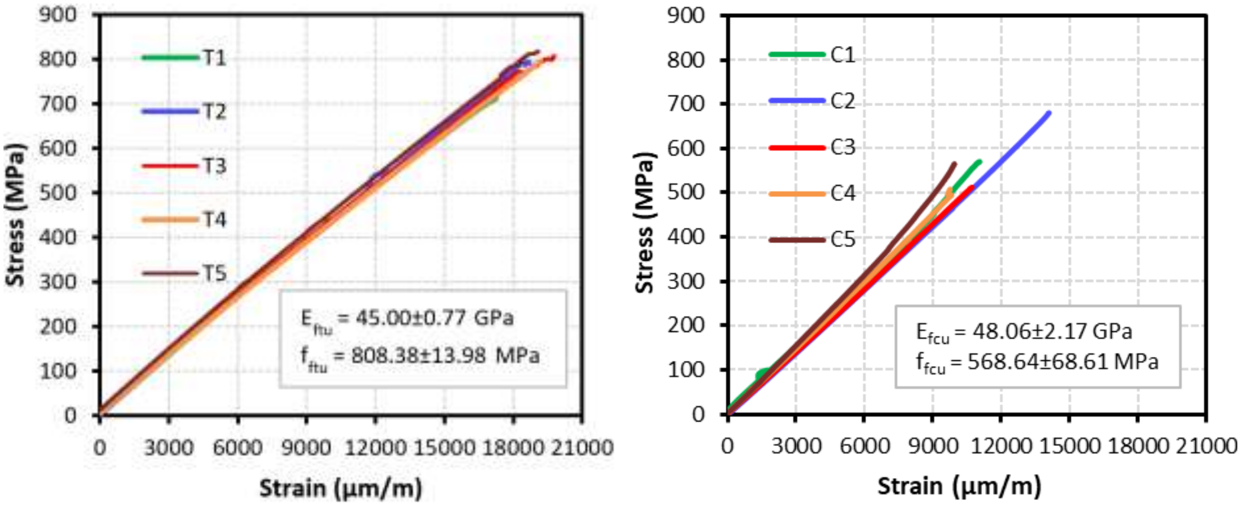

(a) **(b)**

Figure 3. The stress-strain response of the tested GFRP bars in a) Tension and b) Compression

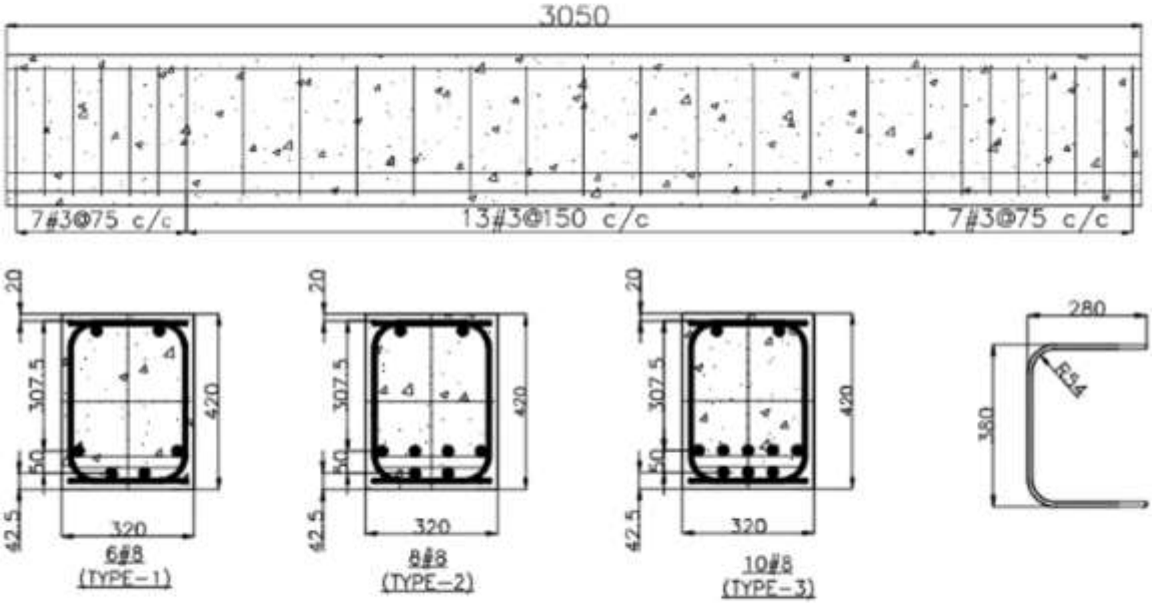

Figure 4. Beam dimensions and reinforcement details (dimension in mm)

Figure 5. GFRP-reinforced concrete beam fabrication

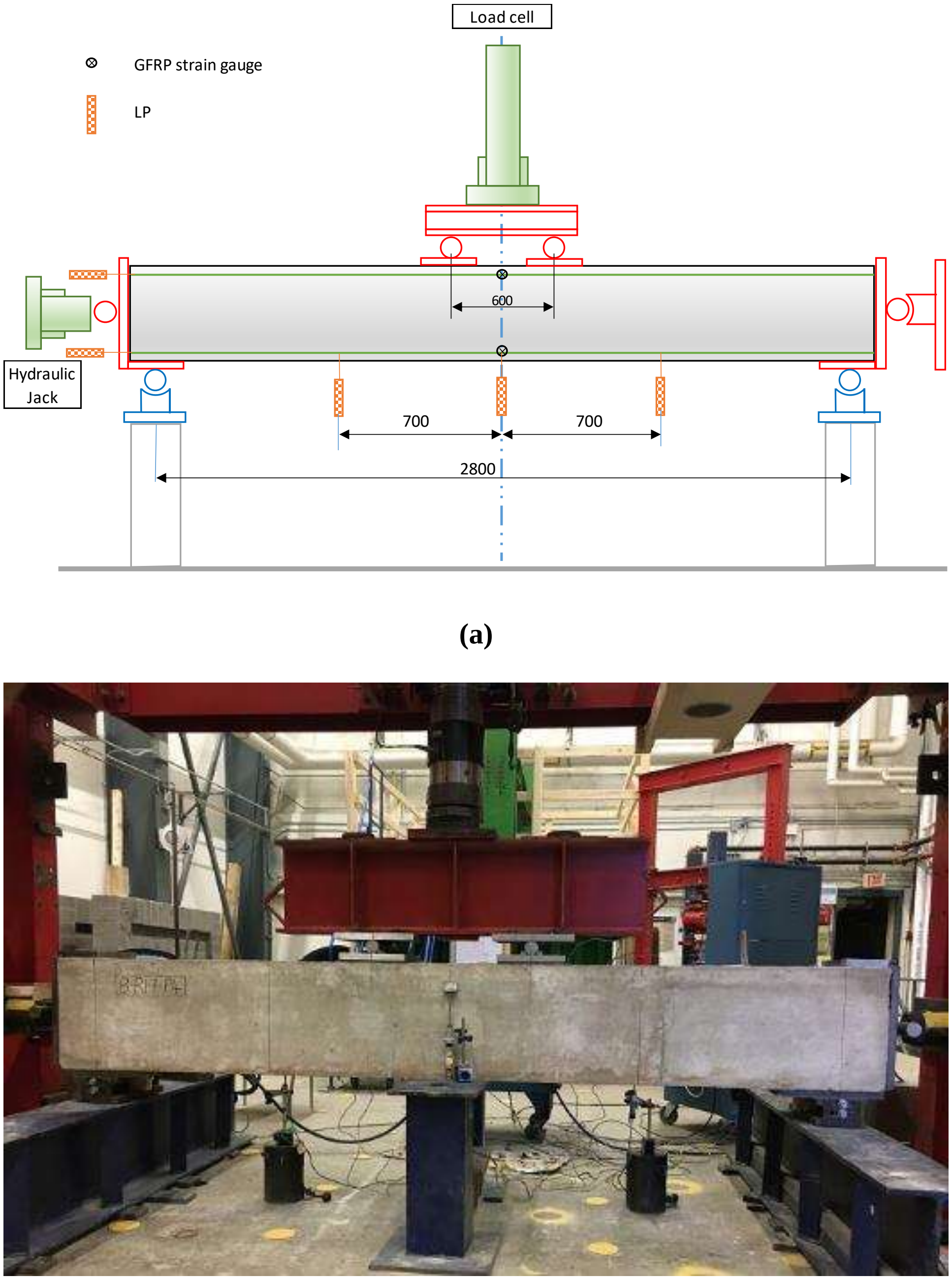

(a)

(b)

Figure 6. GFRP-reinforced concrete beam test set-up and instrumentation details (a) schematic (b) actual (all dimensions are in mm)

B-R1.7-P0

B-R1.7-P2

B-R1.7-P4

Figure 7. Failure Pattern – Beams with 1.7% Reinforcement Ratio (Note: CC is Concrete Crushing, SF is Shear Failure, and FF is Flexural Failure.)

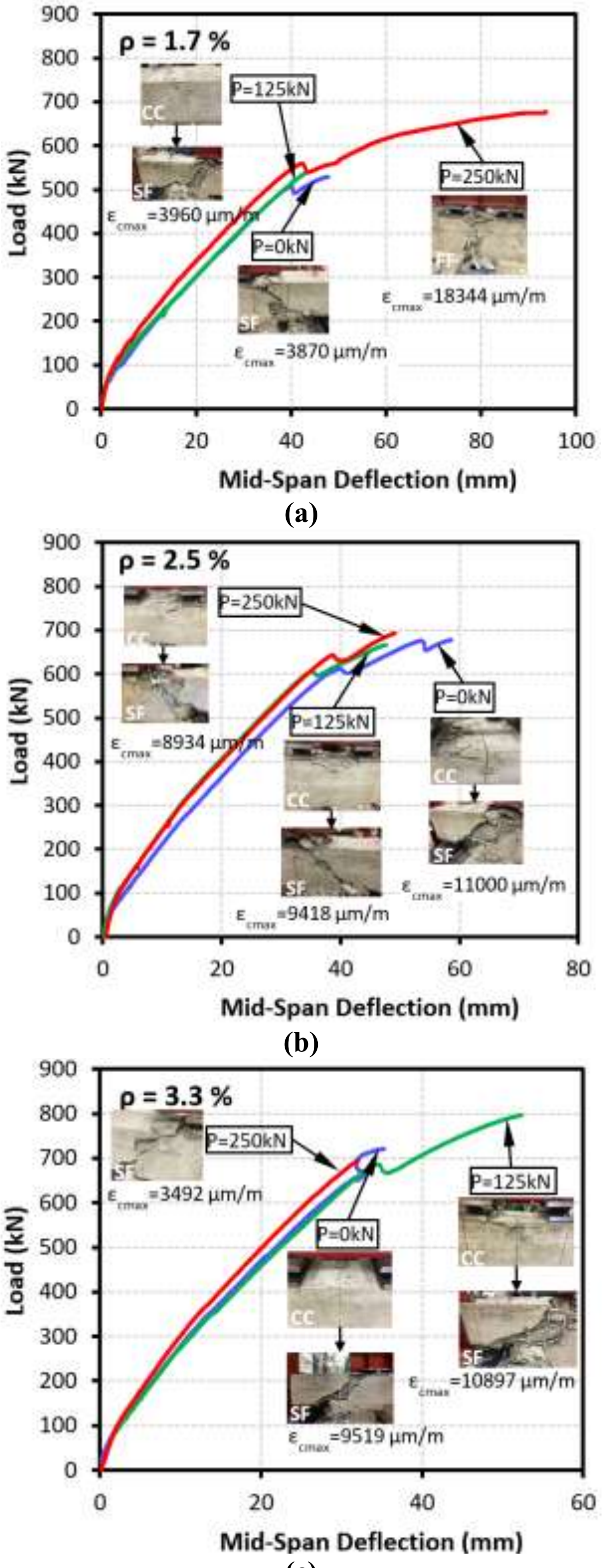

(a)

(b)

(c)

Figure 8. Load vs deflection curve at mid-span (a) ρ = 1.7% (b) ρ = 2.5% (c) ρ = 3.3% (Note: CC is Concrete Crushing, SF is Shear Failure, and FF is Flexural Failure.)

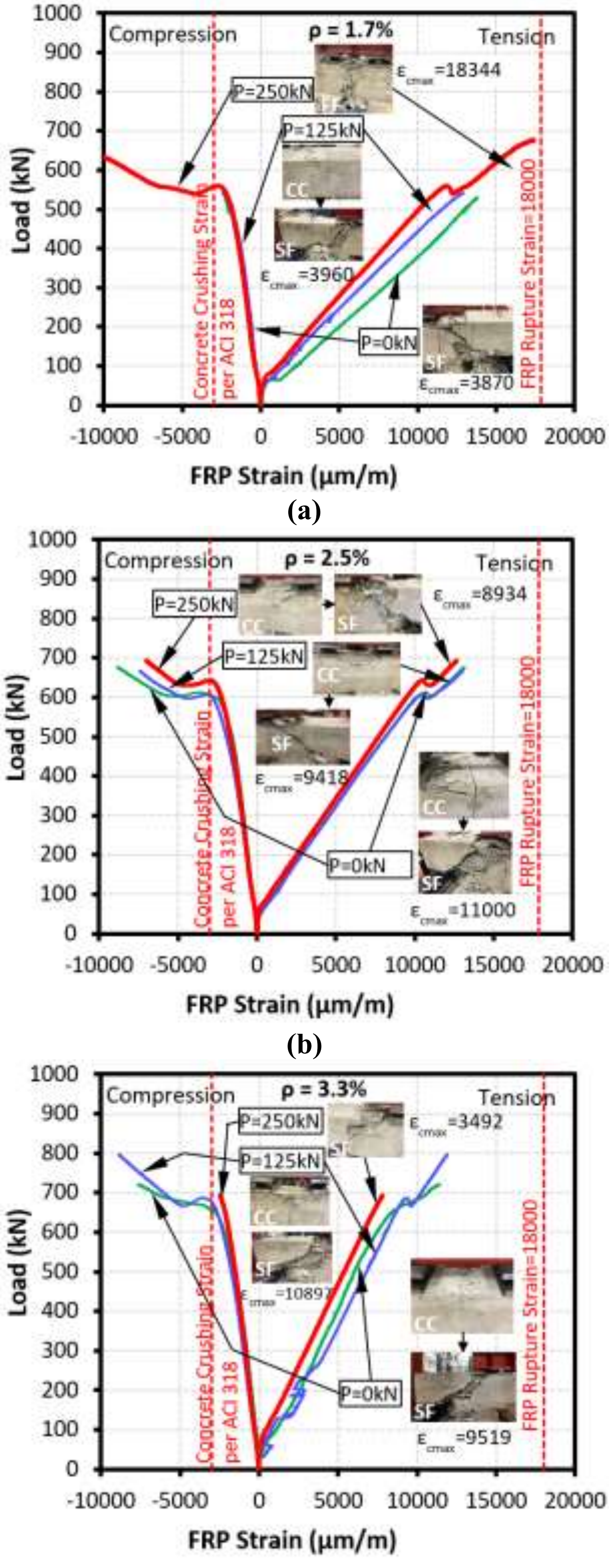

(a)

(b)

(c)

Figure 9. Load vs GFRP strain at mid-span (a) ρ = 1.7% (b) ρ = 2.5% (c) ρ = 3.3%; Note: All the strains are in μm/m

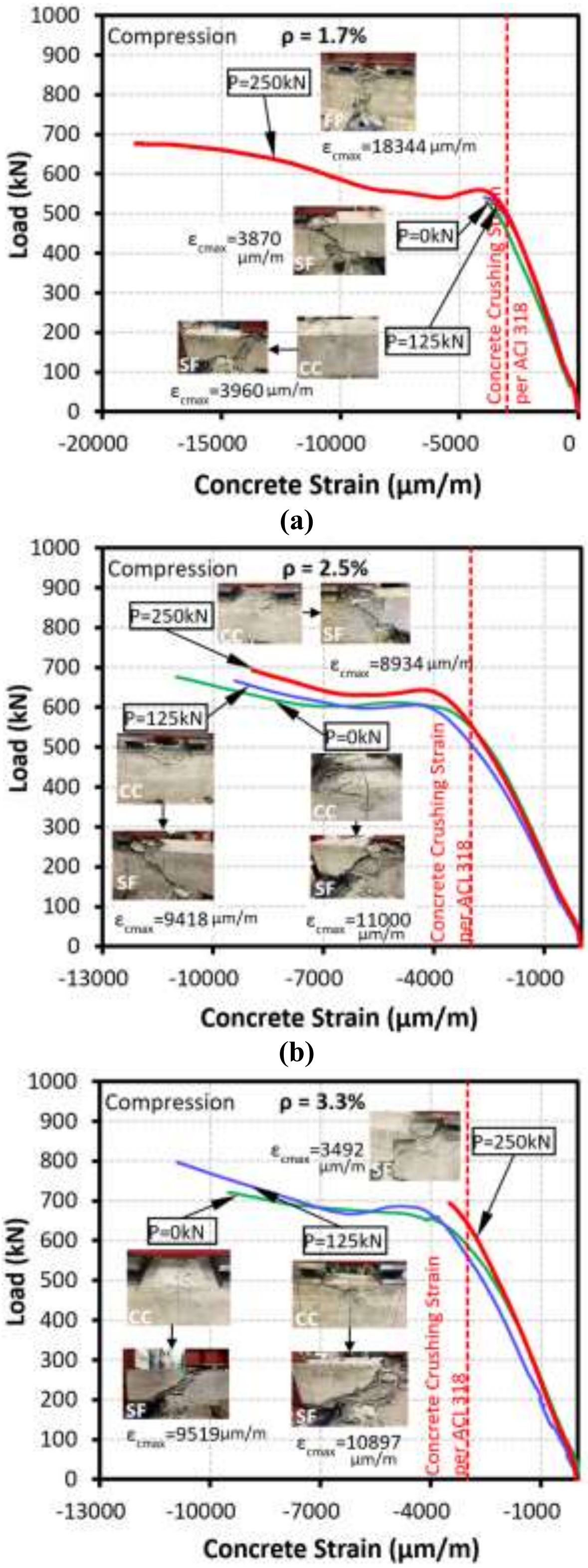

Figure 10. Load vs extreme concrete strain (extrapolated) at mid-span (a) ρ = 1.7% (b) ρ = 2.5% (c) ρ = 3.3%; Note: Strains at concrete are not direct measurements and are extrapolated based on the FRP bar strains

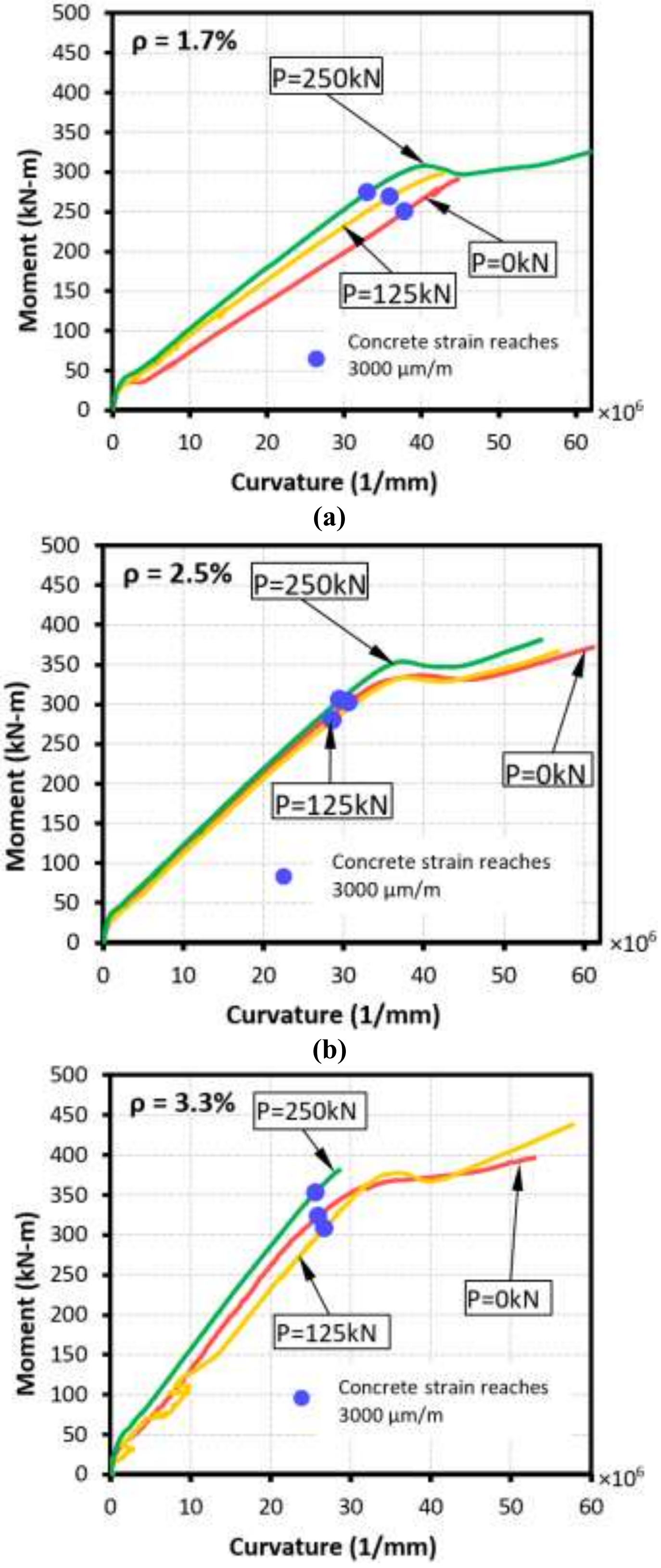

Figure 11. Moment vs Curvature at mid-span (a) ρ = 1.7% (b) ρ = 2.5% (c) ρ = 3.3%

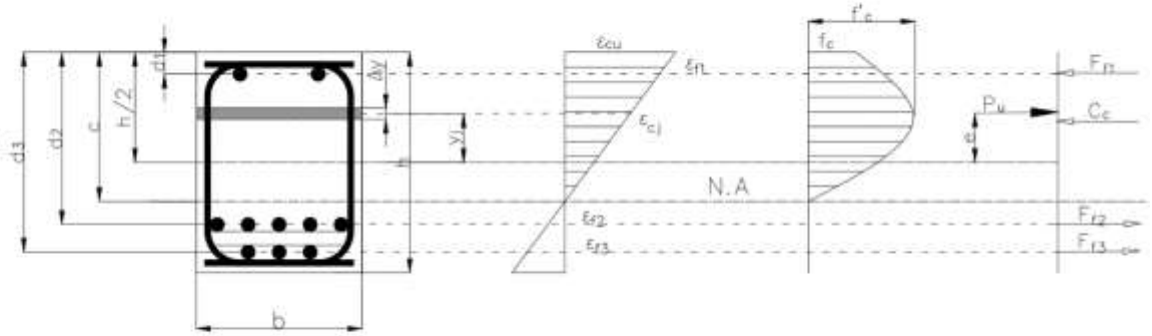

Figure 12. Stress and strain profile of GFRP-reinforced concrete beam cross-section

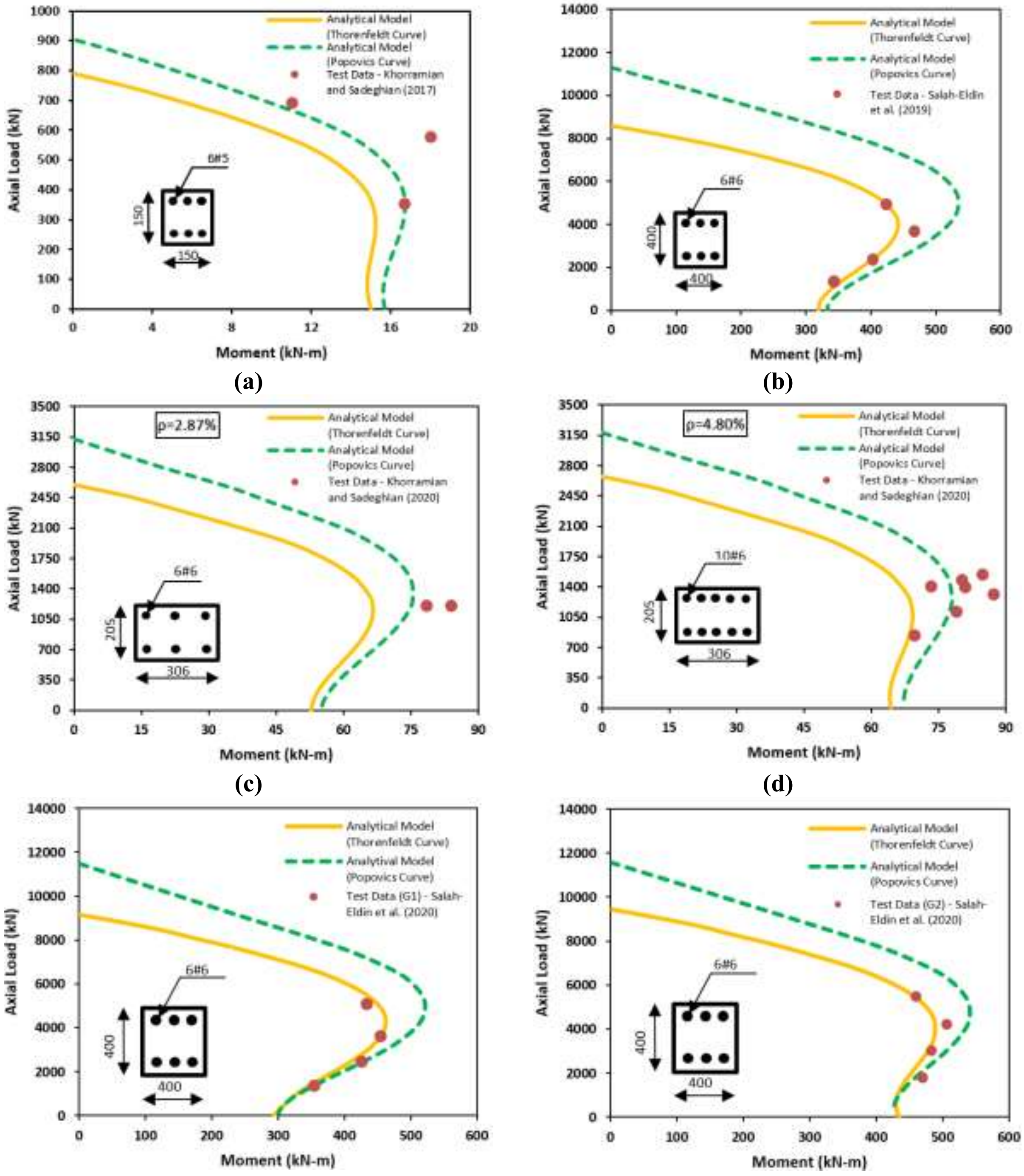

(a) (b) (c) (d) (e) (f)

Figure 13. Comparing beam-column interaction diagram from analytical model and the test data by: a) (Khorramian & Sadeghian, 2017), b) (Salah-Eldin et al., 2019), c and d) (Khorramian & Sadeghian, 2020), e and f) Salah-Eldin et al. (2020)

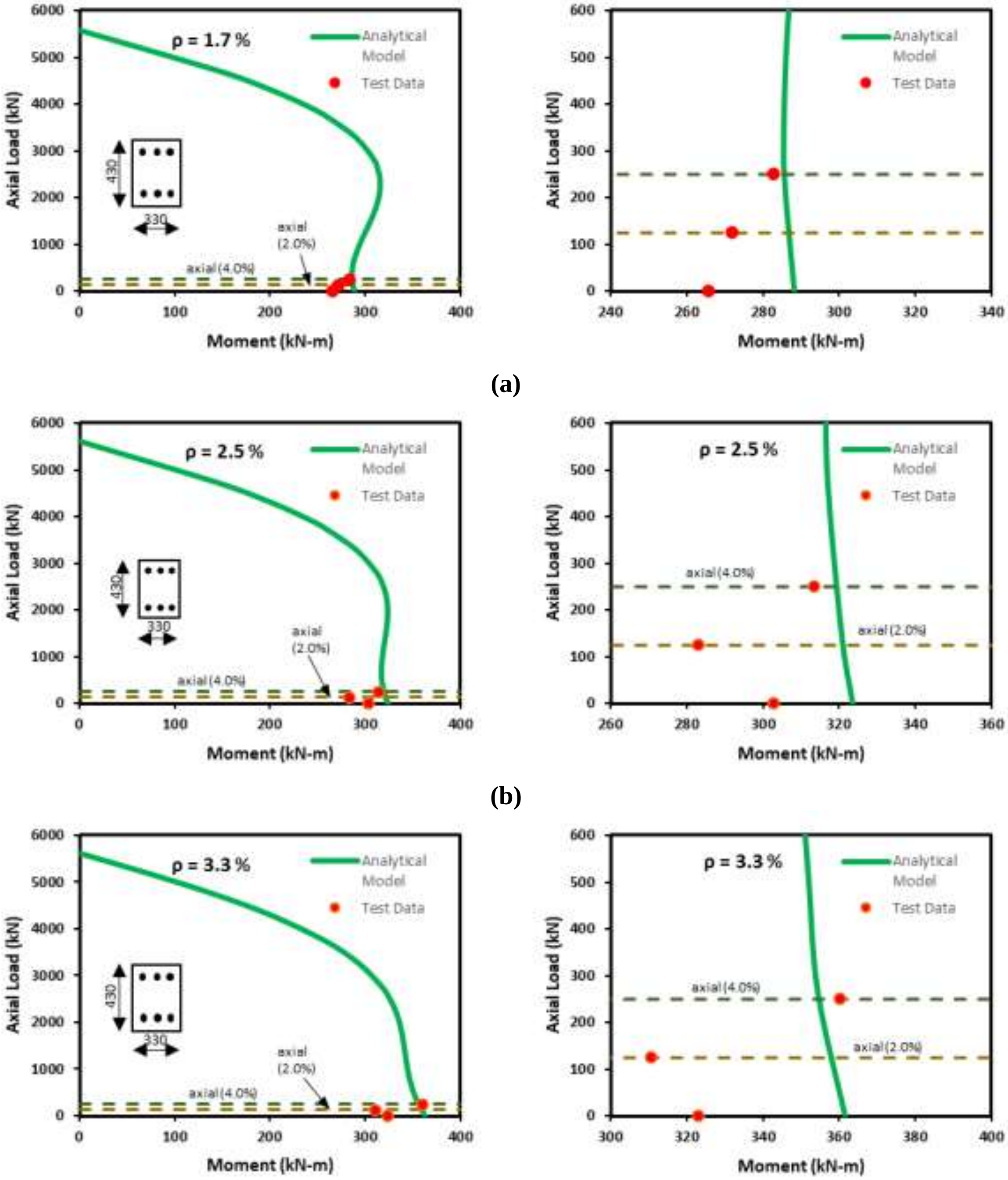

(a)

(b)

(c)

Figure 14. Axial load vs moment (a) ρ = 1.7% (b) ρ = 2.5% (c) ρ = 3.3% (analytical and experimental comparison)

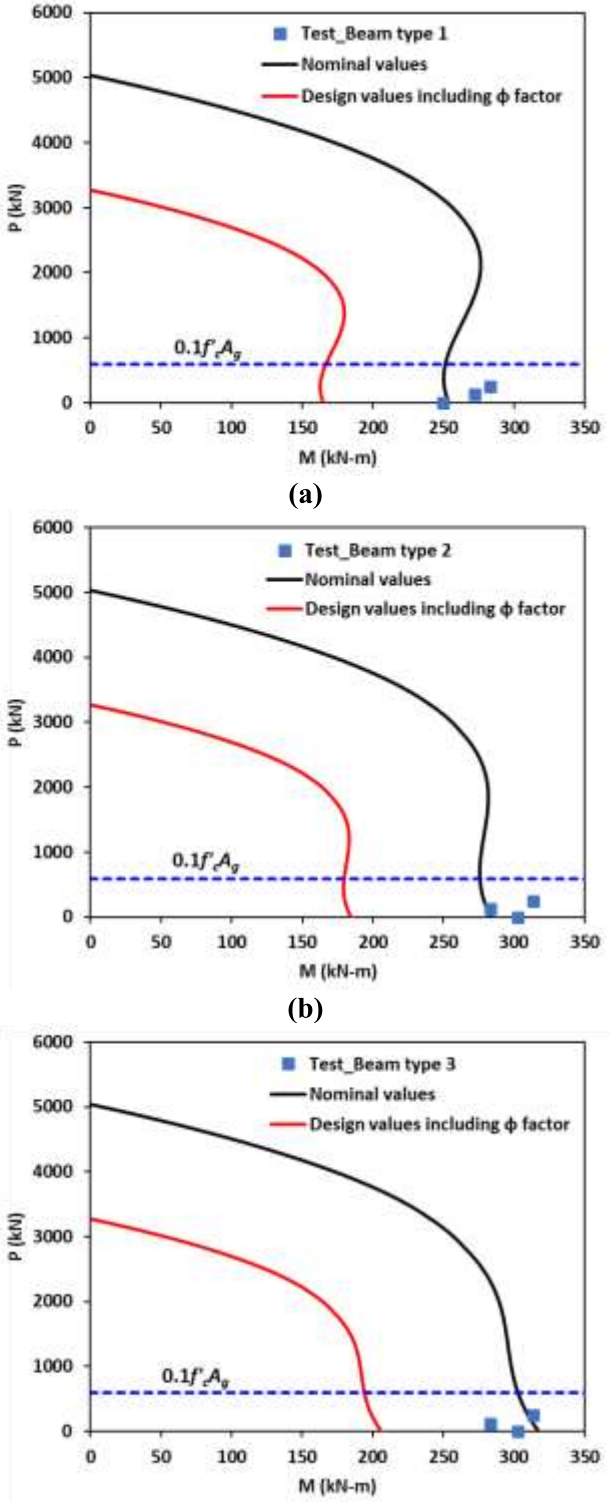

(a)

(b)

(c)

Figure 15. Test data versus interaction diagrams based on equivalent stress block according to ACI-Code 440.11-22 (ACI, 2022): a) ρ=1.7%, b) ρ=2.5%, c) ρ=3.3%

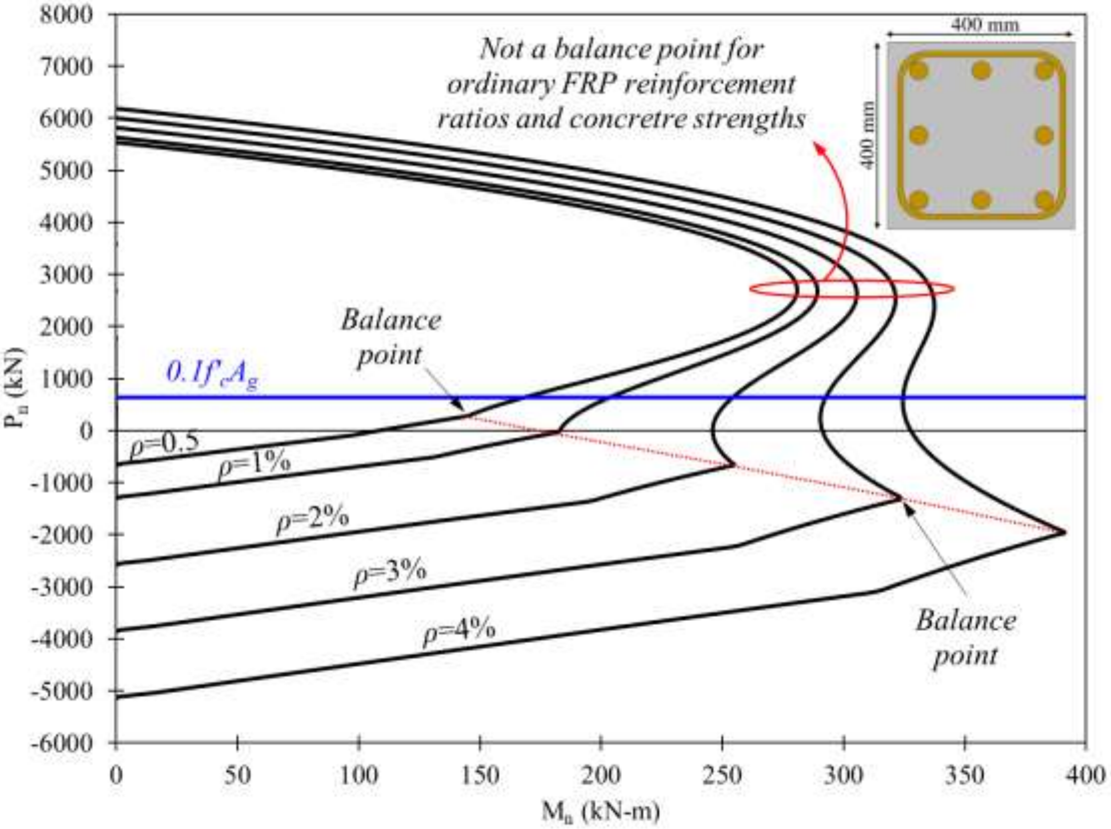

Figure 16. Illustration of different types of interaction diagrams for various reinforcement ratios in an example FRP-reinforced concrete beam-column

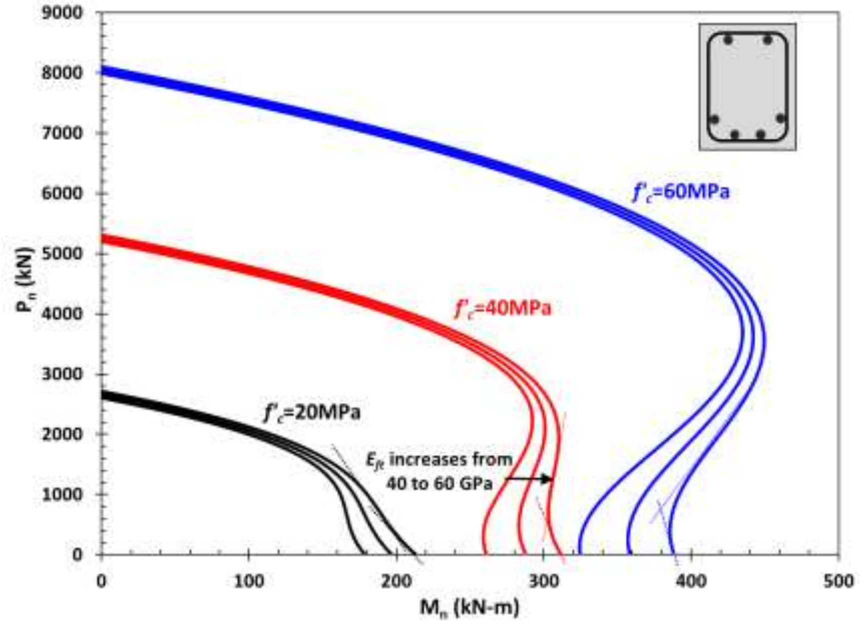
9000
8000
7000
6000
5000
4000
3000
2000
1000
0
P_n (kN)
0
100
200
300
400
500
M_n (kN-m)
f'_c=60MPa
f'_c=40MPa
f'_c=20MPa
E_{ft} increases from 40 to 60 GPa

(a)

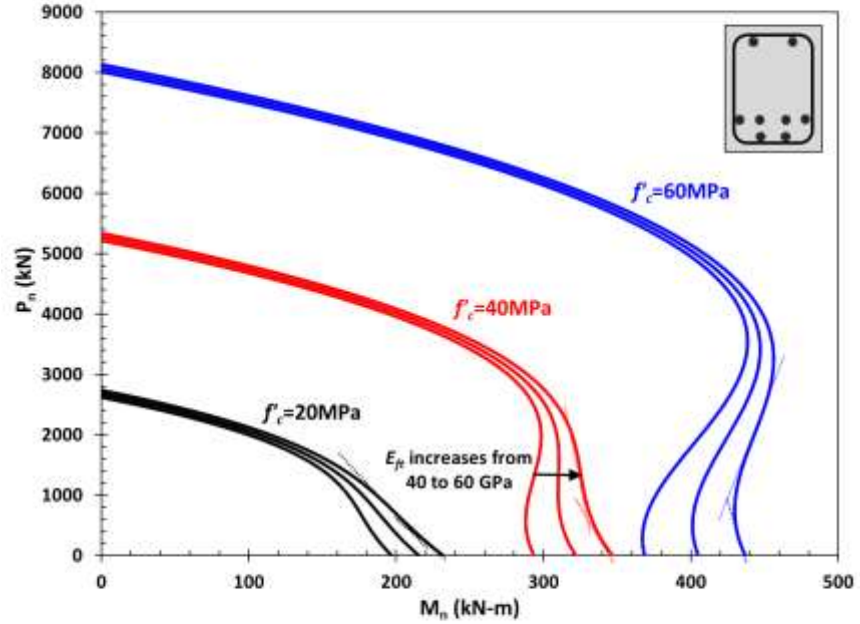
9000
8000
7000
6000
5000
4000
3000
2000
1000
0
P_n (kN)
0
100
200
300
400
500
M_n (kN-m)
f'_c=60MPa
f'_c=40MPa
f'_c=20MPa
E_{ft} increases from 40 to 60 GPa

(b)

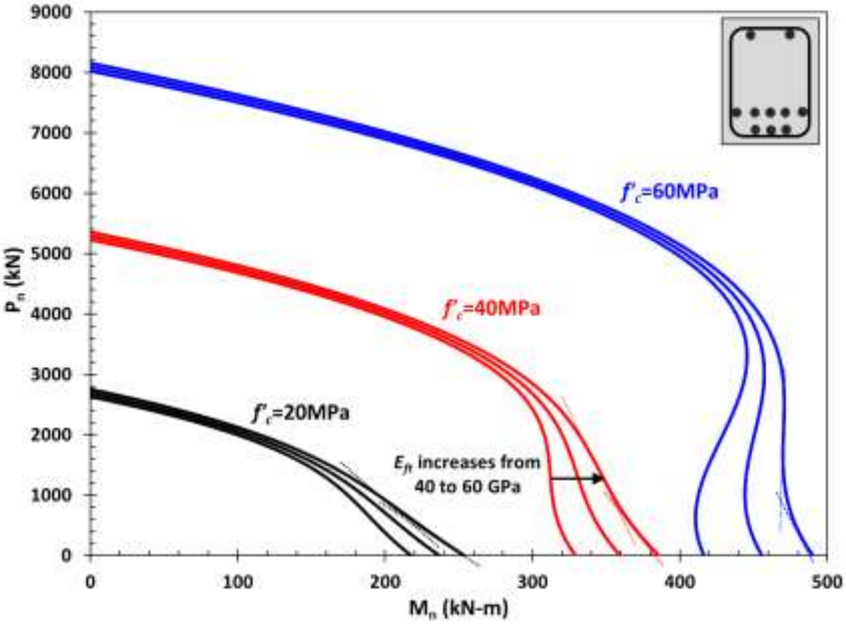

(c)

Figure 17. Interaction diagrams of the beam-column in this study with various material properties for concrete and rebars for parametric studies: reinforcement ratios of a) 1.7%, b) 2.5%, and c) 3.3%